

The physical properties of galaxies with unusually high gas-phase metallicity

Yong-Yun Chen, Qiu-Sheng Gu* and Xue Ge

School of Astronomy and Space Science, Nanjing University, Nanjing 210093, China; qsgu@nju.edu.cn

Received 2019 April 26; accepted 2019 August 13

Abstract We use 1221 galaxies with unusually high gas-phase metallicity to study their physical properties. The scope of redshift is $0.02 < z < 0.25$ for these galaxies with unusually high gas-phase metallicity. Our goal is to understand the physical origins of the high gas-phase metallicity. To address this study, we select a control sample matching similar redshift and stellar mass. Our main results are as follows. (i) Compared with the control sample, the high-metallicity sample shows lower ionization parameter, higher electron density and more dust content. (ii) We also find that the high-metallicity sample has older stellar age and higher [Mgb/<Fe>] ratio, which indicates that the high-metallicity sample has shorter timescale of star formation. (iii) According to the plane of $H\delta_A$ vs. D_n4000 , we can see that the control sample has higher $H\delta_A$ and lower D_n4000 than the high-metallicity sample, which may imply that the control sample experiences recent star formation. (iv) There is a significant difference in gas distribution between the high-metallicity and control samples. The high-metallicity sample has lower gas fraction than control sample, which indicates that galaxies have high gas-phase metallicity probably due to their low HI gas fraction. (v) There is no significant difference between the high-metallicity and control samples in environment, which may suggest that the environment has no effect on gas-phase metallicity.

Key words: galaxies: evolution — galaxies: formation — galaxies: abundance — galaxies: ISM — galaxies: star formation

1 INTRODUCTION

Stellar mass and gas-phase metallicities are important physical parameters for the study of the formation and evolution of galaxies. The stellar mass reflects the amount of gas locked up into stars, while the gas-phase metallicity reflects the gas reprocessed by stars and any gas exchanges between the galaxy and environment (Tremonti et al. 2004). Many authors have studied the relation between stellar mass and gas-phase metallicity in nearby galaxies (e.g., Tremonti et al. 2004; Savaglio et al. 2005; Andrews & Martini 2013; Lian et al. 2015; Bian et al. 2017). The simple closed box chemical evolution model has been used to explain this relation. In this simple case, the galaxies are originally composed of metal-poor gas, and metal-poor gas flows into the galaxies to form stars due to gravitationally collapses (see the review in Tinsley 1980). No gas enters or leaves the galaxy in this scenario. While high metals in high-mass galaxies are mainly due to the feedback from stellar winds and supernova explosion to increase their metal. In a closed box model (Dalcanton

2007), the gas-phase metallicity mainly depends on the gas mass fraction $f_{\text{gas}} (\equiv M_{\text{gas}} / (M_{\text{gas}} + M_{\text{star}}))$. A large amount of metal-poor gas from the intergalactic medium (IGM) flows into the galaxy, diluting the gas-phase metallicity (Larson 1972). The gas-phase metallicity of low mass galaxies may decrease when accretion rate is larger than the star formation rate (i.e., Edmunds 1990; Garnett 2002). However, these excessive accretion events lead to burst of star formation that enriches the galaxy back to the closed box value (Chisholm et al. 2018). Some authors also studied the relation between stellar mass and stellar metallicity (i.e., Gallazzi et al. 2005; Peng et al. 2015). High mass galaxies also have high stellar metallicity. The α/Fe abundance ratio is an important clock to investigate the star formation history in galaxies. Massive galaxies are characterized by systematically higher α/Fe ratio that, together with information on their stellar age, indicates that more massive galaxies formed on shorter timescales and at earlier cosmic epochs than lower mass galaxies, which is the so-called “downsizing” (Thomas et al. 2010).

The scatter of the relation between stellar mass and gas-phase metallicity is an important clue to understand

* Corresponding author

the metal enrichment history of a galaxy. Many studies have found that the relation between stellar mass and metal abundance may be related to other physical parameters, such as star formation rate, D_n4000 (i.e., 4000Å break), galaxy size and morphology (e.g., Ellison et al. 2008; Yates et al. 2012; Andrews & Martini 2013; Lian et al. 2015; Bothwell et al. 2013; Gao et al. 2018). The break occurring at 4000Å is created by absorption lines and was first defined by Bruzual (1983), and redefined by Balogh et al. (1999) as $D_n4000 = \int_{4000}^{4100} f_\lambda d\lambda / \int_{3850}^{3950} f_\lambda d\lambda$. Lian et al. (2015) studied the mass–gas–phase metallicity relation of the Lyman-break analogues (LBAs) in local universe. They found that the mass–gas–phase metallicity relation is dependent on the D_n4000 , which suggests that gas-phase metallicity has a closely link to stellar age. Ellison et al. (2008) found that galaxies of high star formation rate have lower gas-phase metallicity than galaxies of low star formation rate at fixed stellar mass. Subsequently, Mannucci et al. (2010) pointed out a so-called fundamental metallicity relation (FMR), the relation between stellar mass, gas-phase metallicity and star formation rate. They suggested that the scatter in stellar mass–gas–phase metallicity relation could be significantly reduced when consider the star formation rate. Furthermore, it is more important that FMR was found not to evolve out to at least $z = 2.5$ (Mannucci et al. 2010). However, there are always some debates about scatter in the mass–gas–phase metallicity relation. Some authors have thought that the relationship between stellar mass and gas-phase metallicity is not related to star formation rate (e.g., Sánchez et al. 2013, 2017). Some authors also studied the relationship between gas-phase metallicity and environment. Mouhcine et al. (2007) found that the chemical properties of star-forming galaxies are independent of their environments and morphology. Peeples et al. (2008) also found that the environment does not affect the gas-phase metallicity of dwarf galaxies. Cooper et al. (2008) found a relatively weak connection between gas-phase metallicity and environment. Ellison et al. (2008) studied the stellar mass–gas–phase metallicity relation in galaxy clusters. They found that the cluster galaxies in locally rich environments have higher median gas-phase metallicities by up to ~ 0.05 dex than those in locally poor environments. Thomas et al. (2010) studied the environment effect of stellar metallicity in SDSS early-type galaxies. They found that there is no correlation between stellar metallicity and environment. Wu et al. (2017) found that the dependence of stellar mass–gas–phase metallicity relation on the environment is small.

There is growing evidence that the relationship between local galaxies properties and local interstellar medium (ISM) metallicity can help us to better understand the evolution of galaxies. Many physical processes are re-

lated to gas-phase metallicity, such as star formation, gas inflow and outflow. Some authors have suggested that the relation between stellar mass, gas-phase metallicity and gas content is more fundamental than FMR (e.g., Bothwell et al. 2013; Bothwell et al. 2016b,a). The local metal-rich galaxies tend to be gas-poor (Peeples et al. 2008). Peeples et al. (2008) studied a sample of metal-rich dwarfs galaxies. They predicted that their observed high oxygen abundances are due to relatively low gas fraction. Davé et al. (2012) predicted that there is an inverse correlation between gas-phase metallicity and HI mass. Bothwell et al. (2013) found that stellar mass–gas–phase metallicity relation is dependent on mass of atomic hydrogen (HI) by using 4253 local galaxies. Hughes et al. (2013) also found that the mass–gas–phase metallicity relation is dependent on mass fraction of HI gas. Lara-López et al. (2013) also found that metal-rich galaxies have lower gas fraction than metal-poor galaxies. Hwang et al. (2019) used ~ 1000 galaxies observed by Mapping Nearby Galaxies at Apache Point Observatory (MaNGA) to study the relationship between low gas-phase metallicity region of galaxies and the activity of star formation. They found that low gas-phase metallicity region of galaxies tends to have a strong star formation. The reduction of these gas-phase metallicities is mainly due to gas accretion triggering star formation. Brown et al. (2018) used ~ 9000 star-forming galaxies to study the relation between atomic hydrogen (HI), stellar mass and gas-phase metallicity. They proposed that the scatter in the stellar mass–gas–phase metallicity relation is primarily due to gas accretion. At the same time, galaxies also lose metals through galactic outflows when they acquire gas and metals from the intergalactic medium (IGM) (Heckman et al. 1990). Chisholm et al. (2018) suggested that the relation between stellar mass and gas-phase metallicity depends on metal-enriched galactic outflows.

In this work, we study the physical properties of galaxies with unusually high gas-phase metallicity. Our goal is to understand the origin of high gas-phase metallicity. We study the difference of physical parameters between high and low gas-phase metallicity samples, such as ionization parameter, dust content, electron density and so on. We also study the stellar populations of the high and low gas-phase metallicity galaxies using Lick index measurements of key stellar absorption features that probe stellar ages (i.e., D_{4000} , the equivalent width of $H\delta_A$ absorption line), metallicities (i.e., Mgb, MgFe), and α to Fe element abundance ratio.

This paper is structured as follows. In Section 2, we describe how our sample of nearby galaxies is constructed. The results and discussions are shown in Section 3. Finally, Section 4 draws a summary. Throughout this paper, a

Λ CDM cosmology with $H_0 = 70 \text{ km s}^{-1} \text{ Mpc}^{-1}$, $\Omega_m = 0.27$, $\Omega_\Lambda = 0.73$ is adopted.

2 SAMPLE SELECTION

To select galaxies with unusually high gas-phase metallicity, we use the catalogs of SDSS Data Release 7 (DR7) galaxy¹. The SDSS DR7 catalogs contain 927 552 objects with various spectral properties, such as emission-line fluxes and their errors. Our sample selection is based on the following criterion:

1. We require that the signal-to-noise ratio of strong emission line of galaxies is larger than 5 ($S/N > 5$), i.e., $[\text{OIII}]\lambda 5007$, $\text{H}\beta\lambda 4861$, $[\text{NII}]\lambda 6584$, $\text{H}\alpha\lambda 6563$, $[\text{OI}]\lambda 6300$, $[\text{OII}]\lambda\lambda 3726, 29$, $[\text{SII}]\lambda\lambda 6717, 31$, while the weak emission lines have $S/N > 3$, i.e., $[\text{NeIII}]\lambda 3869$. This signal-to-noise ratio limit is to ensure that we get reliable gas-phase metallicity. This results in 41 371 galaxies.
2. We use the BPT diagram (Baldwin et al. 1981) to remove galaxies with the AGN excitations. The criterion was described in Kewley et al. (2001, Ke01) and Kauffmann et al. (2003a, Ka03). At the same time, we also consider that the galaxies have both the measurement of stellar mass and gas-phase metallicity. The range of stellar mass is $8.5 < \log M_* < 11.5$. The redshift measurement is reliable (i.e., $z_{\text{warning}} = 0$) and also $0.02 < z < 0.25$. The redshift limit is to ensure covering $[\text{OII}]\lambda\lambda 3726, 29$. This results in 24 716 galaxies.
3. According to the stellar mass-gas-phase metallicity relation, we use a polynomial fit to the median in bins of 0.1 dex in mass that lie on the 95th percentiles points. The high-metallicity sample was selected as galaxies with gas-phase metallicity lying above the median in bins of 0.1 dex in mass that lie on 95th percentiles points. This results in 1221 high-metallicity galaxies.

To study the physical properties of the high-metallicity sample, we select a control sample. The control sample has gas-phase metallicity lying down 1σ median stellar mass-gas-phase metallicity relation of SDSS star-forming galaxies. At the same time, the control sample has both similar stellar mass and redshift to the high-metallicity sample. The gas-phase metallicity comes from the catalogs of SDSS DR7 galaxy (Tremonti et al. 2004). Figure 1 shows the relation between stellar mass and gas-phase metallicity for the high-metallicity and control samples. From Figure 1, we can see that low mass galaxies have low gas-phase metallicity, while high mass galaxies have

high gas-phase metallicity. One explanation is that supernova explosions produce metal-enriched gas outflow (i.e., Larson 1974; Tremonti et al. 2004; Scannapieco et al. 2008). Low mass galaxies are expected to be more efficient in removing the freshly enriched gas due to the shallower gravitational potential well. Alternatively, low mass galaxies have low gas-phase metallicity owing to the inflow of metal-poor gas that could dilute the gas-phase metallicity (Dalcanton et al. 2004). Another possibility is a mass-dependent star formation efficiency (i.e., Brooks et al. 2007; Calura et al. 2009). In this scenario, more massive galaxies are more efficient in converting their gas reservoirs into stars, which results in lower gas-to-stellar mass ratio and higher gas-phase metallicity. At the same time, it is interesting to note that stellar mass-gas-phase metallicity relation flattens at $M_* > 10^{10} M_\odot$. This phenomenon is predicted naturally by any chemical evolution model. The competing effects between star formation-driven metal production and dilution caused by accretion of pristine gas could lead to the metal enrichment in the gas. Compared with the star formation-driven metal production, the dilution effect is inefficient in the low metallicity regime. Once the gas-phase metallicity becomes high enough, the dilution effect becomes efficient due to gas accretion. Therefore, saturation occurs when the gas-phase metallicity reaches a high enough value for the dilution effect to balance the metal production (Lian et al. 2018).

3 RESULTS AND DISCUSSIONS

3.1 Excitation Mechanism

Figure 2(a) shows the $\log [\text{OIII}]/\text{H}\beta$ as a function of $\log [\text{NII}]/\text{H}\alpha$ standard optical diagnostic diagram for the high-metallicity (red contour) and control sample (black contour). The blue dashed and green solid lines show the classification lines of Ka03 and Ke01, respectively. Galaxies that lie below the blue dashed line are classed as HII-region-like galaxies. From Figure 2(a), we find that the $\log [\text{NII}]/\text{H}\alpha$ ratio of the high-metallicity sample is higher than control sample by ~ 0.5 dex. The $\log [\text{OIII}]/\text{H}\beta$ ratio of the high-metallicity sample is lower than control sample by ~ 0.5 dex. The control and high-metallicity samples form a tight sequence from low metallicities (low $\log [\text{NII}]/\text{H}\alpha$, high $\log [\text{OIII}]/\text{H}\beta$) to high metallicities (high $\log [\text{NII}]/\text{H}\alpha$, low $\log [\text{OIII}]/\text{H}\beta$).

Because the $[\text{NII}]\lambda 6584$ flux could be enhanced by shocks and/or AGNs in galaxies. Thus, we also use other diagnostic lines that are sensitive to the shocks and/or AGNs, including the $[\text{SII}]\lambda\lambda 6717, 6731$, $[\text{OI}]\lambda 6300$ emission lines. Figure 2(b) and (c) show the $\log [\text{OIII}]/\text{H}\beta$ as a function of $\log [\text{SII}]/\text{H}\alpha$ and $\log [\text{OIII}]/\text{H}\beta$ as a function of $\log [\text{OI}]/\text{H}\alpha$ diagrams for the high-metallicity (red

¹ https://wwwmpa.mpa-garching.mpg.de/SDSS/DR7/raw_data.html

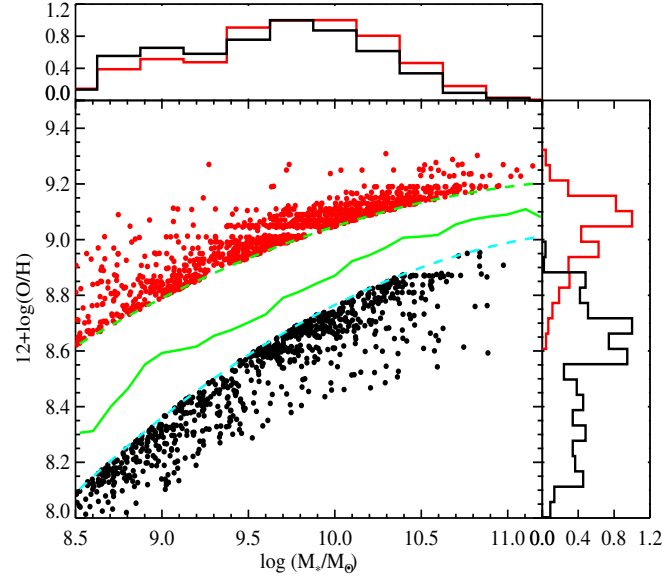


Fig. 1 Relation between stellar mass and gas-phase metallicity for the high-metallicity (*red dot*) and control (*black dot*) samples. The *green solid line* indicates a median stellar mass-gas-phase metallicity of SDSS DR7 star-forming galaxies. The *green dashed line* shows a polynomial fit to the median in bins of 0.1 dex in mass that lie on the 95th percentiles points. The *cyan dashed line* shows a polynomial fit to the median in bins of 0.1 dex in mass that lying on the 16th percentiles points (1σ). The *red histogram* indicates the distribution of stellar mass and gas-phase metallicity for the high-metallicity samples. The *black histogram* indicates the distribution of stellar mass and gas-phase metallicity for control sample.

contour) and control sample (black contour), respectively. We find that the high-metallicity and control samples lie below the green solid line, which suggests that the high-metallicity and control samples are not contaminated by AGNs or strong shocks. The high-metallicity sample has relatively lower $\log [\text{SII}]/\text{H}\alpha$ ratio than control sample by ~ 0.1 dex. The $\log [\text{OI}]/\text{H}\alpha$ ratio of the high-metallicity sample is lower than control sample by ~ 0.2 dex. We also note that 0.1 dex is not a large difference. At the same time, the high-metallicity sample is far away from the green solid line, while the control sample is close to the green solid line. These results suggest that the high-metallicity sample may have lower ionization state than control sample.

Figure 2(d) shows $\log [\text{OIII}]/\text{H}\beta$ as a function of $\log [\text{OIII}]/[\text{OII}]$ for the high-metallicity (red contour) and control samples (black contour). From Figure 2(d), we find that the high-metallicity sample has relatively lower $\log [\text{OIII}]/\text{H}\beta$ ratio than control sample by ~ 0.7 dex. The $\log [\text{OIII}]/[\text{OII}]$ ratio of the high-metallicity sample is lower than control sample by ~ 0.5 dex. Because $\log [\text{OIII}]/[\text{OII}]$ can be used as an indicator of ionization state. Thus, we can see that the high-metallicity and control samples seem to form a single sequence from low ionization to high ionization state.

3.2 Spectral Energy Distribution

Richardson et al. (2016) proposed the spectral energy distribution (SED) diagnostic diagrams, which uses the ratios of different emission lines from different ionization states; i.e., $[\text{OI}]$, $[\text{OII}]$, and $[\text{OIII}]$ emission line ratios. The ionization energies of $[\text{OI}]$, $[\text{OII}]$ and $[\text{OIII}]$ are 13.6, 35.1 and 54.9 eV, respectively. Figure 3(a) shows the $\log [\text{OIII}]/[\text{OII}]$ as a function of $\log [\text{OII}]/[\text{OI}]$. The high-metallicity sample tends to have a lower ratio of $\log [\text{OIII}]/[\text{OII}]$ than control sample. Levesque & Richardson (2014) pointed out that the ratio of $[\text{NeIII}]/[\text{OII}]$ can be used as a tracer of ionization parameter for high redshift star-forming galaxies. In Figure 3(b), the high-metallicity and control samples are shown in the plane of $\log [\text{NeIII}]/[\text{OII}]$ versus $\log [\text{OIII}]/[\text{OII}]$. The high-metallicity sample also tends to have lower $\log [\text{NeIII}]/[\text{OII}]$ than control sample by ~ 0.1 dex, which suggests that the high-metallicity sample has lower ionization state than control sample. However, we also note that 0.1 dex is not significant difference.

In Figure 4, we plot the $\log [\text{OIII}]/[\text{OII}]$ ratio as a function of $\log \text{H}\alpha$ luminosity (a) and $\log [\text{OIII}]$ luminosity (b) of galaxies. Compared with control sample, the high-metallicity sample tends to have lower $\log [\text{OIII}]$ luminosity by ~ 0.07 dex. The 0.07 dex is not a large difference. The $\log [\text{OIII}]/[\text{OII}]$ ratio of control sample rises

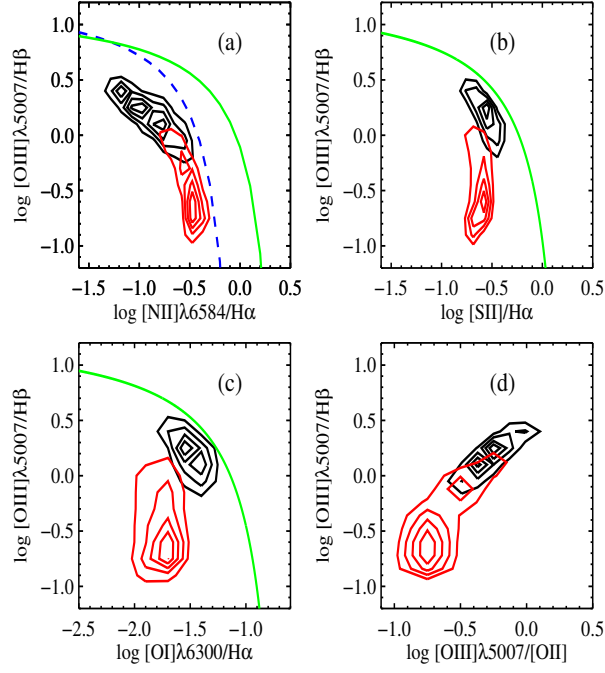


Fig. 2 The optical diagnostic diagram of the high-metallicity (*red contour*) and control (*black contour*) samples. (a) The $\log [\text{OIII}]/\text{H}\beta$ as a function of $\log [\text{NII}]/\text{H}\alpha$; (b) the $\log [\text{OIII}]/\text{H}\beta$ as a function of $\log [\text{SII}]/\text{H}\alpha$; (c) the $\log [\text{OIII}]/\text{H}\beta$ as a function of $\log [\text{OI}]/\text{H}\alpha$; (d) the $\log [\text{OIII}]/\text{H}\beta$ as a function of $\log [\text{OIII}]/[\text{OII}]$. The *blue dashed line* is the Ka03 (Kauffmann et al. 2003a) classification line. The *green solid line* is the Ke01 (Kewley et al. 2001) extreme starburst line.

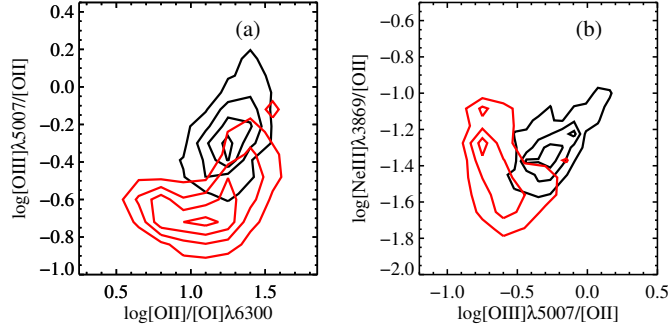


Fig. 3 The spectral energy distribution of ionization radiation for the high-metallicity (*red contour*) and control (*black contour*) samples. (a) $\log [\text{OIII}]/[\text{OII}]$ as a function of $\log [\text{OII}]/[\text{OI}]$; (b) $\log [\text{NeIII}]/[\text{OII}]$ as a function of $\log [\text{OIII}]/[\text{OII}]$.

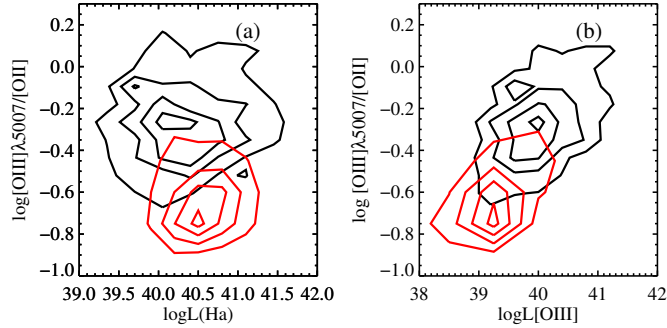


Fig. 4 The $\log [\text{OIII}]/[\text{OII}]$ as function of $\log \text{H}\alpha$ line luminosity (a) and $\log [\text{OIII}]$ luminosity (b) for the high-metallicity (*red contour*) and control (*black contour*) samples.

significantly when the luminosity of $\log [\text{OIII}]\lambda 5007$ larger than 39.5.

3.3 Gas-phase Metallicity

The electron temperature (T_e) method is the most reliable approach to estimate the gas-phase metallicity, which is based on the ratios of faint auroral-to-nebular emission lines (Lin et al. 2017), such as $[\text{OIII}]\lambda 4363/[\text{OIII}]\lambda 5007$. However, auroral lines are weak in galaxies, such as $[\text{OIII}]\lambda 4363$ lines, especially for the galaxies of high gas-phase metallicity. A lot of calibrators can also be used to estimate the gas-phase metallicity besides the electron temperature (T_e) method (Kewley & Ellison 2008). According to the photoionization models for HII regions, some emission lines ratios can also be used as the calibrators to reproduce the gas-phase metallicity, such as $([\text{OII}]\lambda 3727 + [\text{OIII}]\lambda 4959, 5007)/\text{H}\beta$ (R23; Kobulnicky & Kewley 2004), $[\text{NII}]\lambda 6584/[\text{OII}]\lambda 3727$ (N2O2; Kewley & Dopita 2002), $([\text{OIII}]\lambda 5007/\text{H}\beta)/([\text{NII}]\lambda 6583/\text{H}\alpha)$ and $[\text{NII}]\lambda 6583/\text{H}\alpha$ (O3N2, N2; Pettini & Pagel 2004). However, there is a large difference between the gas-phase metallicity derived by different calibrators (Kehrig et al. 2013). For example, compared with the N2O2 diagnostic, O3N2 and N2 almost could not reproduce the supersolar oxygen abundances and would derive lower metallicity (Blanc et al. 2015; Zhang et al. 2017). Dopita et al. (2013) have proposed that the N2O2 is optimal indicator of gas-phase metallicity because it is not sensitive to the ionization parameter. Therefore, we also use the $[\text{NII}]/[\text{OII}]$ ratios as a tracer of gas-phase metallicity besides R23 methods. Figure 5 shows ratios of lines with similar ionization potentials. In Figure 5(a), the high-metallicity and control samples are shown in the plane of $\log [\text{NII}]/\text{H}\alpha$ vs. $\log [\text{SII}]/\text{H}\alpha$. Figure 5(b) shows the $\log [\text{NII}]/[\text{OII}]$ as a function of $\log [\text{OI}]/\text{H}\alpha$ for the high-metallicity and control samples. The $\log [\text{NII}]/[\text{OII}]$ ratio of the high-metallicity sample is higher than control sample by ~ 0.6 dex. We find that the high-metallicity sample has really higher gas-phase metallicity than control sample. Our results are independent of the gas-phase metallicity calibrators.

3.4 Electron Density and Ionization Parameter

Shimakawa et al. (2015) found that electron densities are correlated with specific star formation rate. Some authors have suggested that there is a relation between gas-phase metallicity and star formation rate (i.e., Ellison et al. 2008; Yates et al. 2012; Andrews & Martini 2013). Thus, we also study the electron densities of the high-metallicity and control samples. Osterbrock (1989) suggested that the emission-line flux ratios of $[\text{SII}]\lambda 6717/\lambda 6731$ can be used

as a tracer of the electron density, low ratio means higher electron densities. The $[\text{OIII}]\lambda 5007/[\text{OII}]\lambda 3727$ flux ratio is a useful indicator of ionization parameter (e.g., Komossa & Schulz 1997; Nagao et al. 2002).

Figure 6 shows the $\log [\text{SII}]\lambda 6717/\lambda 6731$ as a function of $\log [\text{OIII}]\lambda 5007$ luminosity (a) and the $\log [\text{OIII}]/[\text{OII}]$ ionization parameter (b) for the high-metallicity and control samples. As seen previously, the high-metallicity sample is offset towards lower $\log [\text{OIII}]\lambda 5007$ luminosities and ionization parameters compared to control sample. From this figure, we can see that the high-metallicity sample tends to have higher electron density than control sample by ~ 0.05 dex.

The histograms of electron density (a) and ionization parameter (b) are shown in Figure 7. From Figure 7, we can see that the high-metallicity sample has lower $\log [\text{SII}]\lambda 6717/[\text{SII}]\lambda 6731$ than control sample by ~ 0.05 dex. The $\log [\text{OIII}]/[\text{OII}]$ ratios of the high-metallicity sample is lower than control sample by ~ 0.5 dex. These results suggest that the high-metallicity sample has high electron density and lower ionization parameter than control sample. We also note that 0.05 dex is not a large difference. Using the Kolmogorov-Smirnov (K-S) test, both of the electron densities and ionization parameter distributions of the high-metallicity and control samples yield p-values of $p < 0.001$, which indicates a significant difference between the high-metallicity and control samples in electron density and ionization parameter. Nagao et al. (2006) found that high-metallicity galaxies have a relatively low-ionization parameters. Many authors have found that young and extremely metal-poor starburst galaxies have high ionization parameter (e.g., Fosbury et al. 2003; Erb et al. 2010; Richard et al. 2011). Kashino & Inoue (2019) found that ionization parameter (U) is primarily controlled by sSFR, as $U \propto \text{sSFR}^{0.43}$. The partial dependence of U on electron density (n_e) is found to be $U \propto n_e^{-0.29}$. Our results may suggest that the high-metallicity sample has weak star-formation activity (low SFR, sSFR).

3.5 Stellar Populations

3.5.1 Stellar population age and metallicity

1. We use the 4000 Å break ($D_n 4000$) and the $\text{H}\delta_A$ absorption lines as indicators of the age of the stellar population. The strength of 4000 Å break is influenced by temperature and metallicity (Kewley et al. 2006). The $D_n 4000$ can be used as a tracer of the galaxy age for galaxies with mean stellar ages less than a few Gyrs.
2. The other age indicator is the equivalent width (EW) of the $\text{H}\delta_A$ absorption line. Strong $\text{H}\delta_A$ absorption line indicates that galaxies experience a burst of star

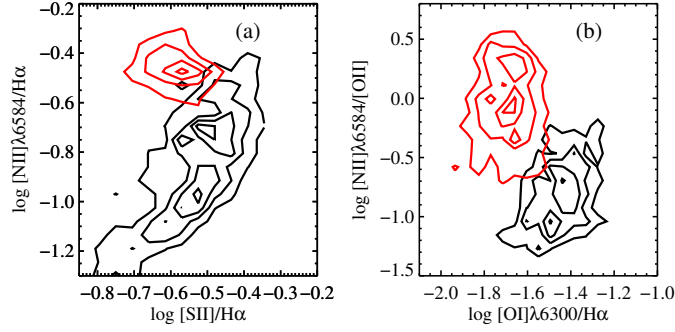


Fig. 5 The diagnostic diagrams of metal abundances for the high-metallicity (*red contour*) and control (*black contour*) samples. (a) $\log [\text{NII}]/\text{H}\alpha$ as a function of $\log [\text{SII}]/\text{H}\alpha$; (b) $\log [\text{NII}]/[\text{OII}]$ as a function of $\log [\text{OI}]/\text{H}\alpha$.

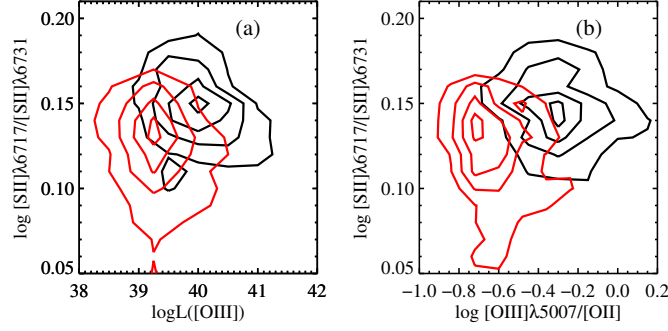


Fig. 6 The electron density diagnostic $[\text{SII}]\lambda 6717/[\text{SII}]\lambda 6731$ ratio is plotted as a function of $[\text{OIII}]$ luminosity (a) and $[\text{OIII}]/[\text{OII}]$ ionization parameter (b). *Red contour* indicates the high-metallicity sample, and *black contour* shows the control sample.

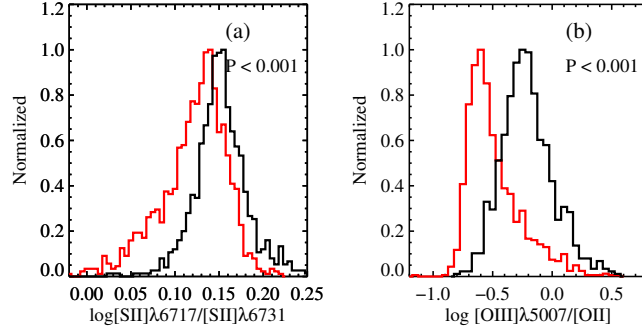


Fig. 7 The histograms of electron density diagnostic $[\text{SII}]\lambda 6717/[\text{SII}]\lambda 6731$ ratio (a) and $[\text{OIII}]/[\text{OII}]$ ionization parameter (b). *Red histogram* is the high-metallicity sample, and *black histogram* shows the control sample. The value of p indicates the significance level of K-S statistic.

formation that ended $\sim 0.1\text{--}1$ Gyr ago (Worthey & Ottaviani 1997). Worthey & Ottaviani (1997) defined the $\text{H}\delta_A = (4083.50 - 4122.25)/(1 - (F_I/F_C))$, where F_I is the flux within 4083.50–4122.25 bandpass and F_C is the pseudo-continuum flux within the bandpass. Kauffmann et al. (2003b) suggested that the $D_n 4000\text{--}\text{H}\delta_A$ plane could be used to distinguish whether galaxies have been forming stars continuously or in bursts over the past 1–2 Gyr.

3. The total stellar metallicity can be indicated by using the index, $[\text{MgFe}]'$. Thomas et al. (2003) proposed that

the $[\text{MgFe}]'$ could be calculated by the following formula:

$$[\text{MgFe}]' = \sqrt{\text{Mgb}(0.72\text{Fe}5270 + 0.28\text{Fe}5335)}. \quad (1)$$

4. The α -enhancement of the stellar population can be indicated by using $[\alpha/\text{Fe}]$. The $[\alpha/\text{Fe}]$ is estimated using the following formula:

$$[\alpha/\text{Fe}] = -1.030 + 1.016X - 0.141X^2, \quad (2)$$

where $X = \text{Mgb}/\langle\text{Fe}\rangle$, $\langle\text{Fe}\rangle = \text{Fe}5270 + \text{Fe}5335$ combination (Thomas et al. 2003).

Figure 8 shows the $H\delta_A$ as a function of D_n4000 , Mgb as a function of D_n4000 , $[MgFe]'$ as a function of D_n4000 , and $[\alpha/Fe]$ as a function of $H\delta_A$, respectively. Figure 8(a) shows the relation between $H\delta_A$ and D_n4000 . We find that control sample has lower D_n4000 than the high-metallicity sample by ~ 0.03 dex. The $H\delta_A$ of control sample is higher than the high-metallicity sample by ~ 0.8 dex, which suggests that control sample likely experiences recent star formation. Figure 8(b) and (c) show the stellar metallicity as a function of D_n4000 . The high-metallicity sample has higher stellar metallicity than control sample by ~ 0.3 dex. Figure 8(d) shows the $[\alpha/Fe]$ as a function of $H\delta_A$ for the high-metallicity and control samples. The high-metallicity sample has higher $[\alpha/Fe]$ ratio than control sample by ~ 0.03 dex, indicating that their stellar populations are more enhanced with α -elements. Although the 0.03 dex is not large difference. However, the high-metallicity and control samples have significant difference in the distribution of D_n4000 , $H\delta_A$, Mgb, $[MgFe]'$ and $[\alpha/Fe]$ based on K-S test.

3.5.2 Relationship between stellar age, metallicity and ionization state

Figure 9 shows the $H\delta_A$ as a function of D_n4000 , Mgb as a function of D_n4000 , $[MgFe]'$ as a function of D_n4000 , and $\log [OIII]/[OII]$ luminosity as a function of D_n4000 for the high-metallicity sample, the colorbar shows the $\log [OIII]/[OII]$ ratios. From this figure, we see that the galaxies with low $\log [OIII]/[OII]$ values have old, metal-rich stellar populations. Galaxies with young stellar populations have high $\log [OIII]$ luminosity.

In Figure 10, we plot the high-metallicity and control samples in the plane of $\log [NeIII]/[OII]$ as a function of $\log [OIII]/[OII]$ according to their D_n4000 values, respectively. Galaxies with old stellar populations have relatively low $[OIII]/[OII]$ ratio in both the high-metallicity and control samples. The galaxies with recent star formation (low D_n4000) have high $[OIII]/[OII]$ values in both samples. However, galaxies with old stellar populations occupy a wide range in $\log [NeIII]/[OII]$ ratio in the high-metallicity sample. The relation between D_n4000 and $\log [NeIII]/[OII]$ is more complex.

3.5.3 Relationship between $[OIII]$ luminosity and ionization state

In Figure 11, we colour-code galaxies in the plane of $\log [NeIII]/[OII]$ as a function of $\log [OIII]/[OII]$ according to their $\log [OIII]$ luminosity. The high-metallicity sample is shown in left-hand panel and control sample is shown in the right-hand panel, respectively. Galaxies with high $\log [OIII]$ luminosities have high ionization state

in both samples. In the previous subsection, we found that galaxies with young stellar populations have high ionization state and $\log [OIII]$ luminosities. Usually, the $\log [OIII]$ luminosity is also used to indicate the activity of the central supermassive black hole. We have found that the galaxies with recent star formation have young stellar population, high ionization state, and high $\log [OIII]$ luminosities, which suggests that they are likely accreting gas to trigger the activity of the central black hole.

3.6 Relationship between Color and Stellar Mass

The optical band data of SDSS galaxies come from the catalog of Chilingarian et al. (2017). The near-ultraviolet (NUV) data derive from the catalog of Martin et al. (2005). The mid-infrared data come from the catalog of Wright et al. (2010). The star formation rate (SFR) and stellar mass of galaxies are adopted from the Max-Planck-Institute for Astrophysics (MPA)/Johns Hopkins University (JHU) DR7 Value Added Galaxy Catalogue (VAGC) (Brinchmann et al. 2004; Kauffmann et al. 2003b; Salim et al. 2007).

Figure 12 shows the relation between colors and stellar mass for the high-metallicity and control samples. (a) Optical colors versus stellar mass; (b) near-UV colors versus stellar mass; (c) mid-IR color versus stellar mass; (d) Balmer decrement ($H\alpha/H\beta$) versus stellar mass. Red dots are the high-metallicity samples, and black dots are control samples. Large red circles are medians of the high-metallicity samples. Large black squares are medians of control samples. Blanton et al. (2003) suggested that the optical $g - r$ color is an indicator of star formation activity in galaxies. At the same time, the NUV- r and $[3.4] - [12]$ colors are also used to indicate the recent star formation activity of galaxies (e.g., Ko et al. 2013; Lee et al. 2015). The $H\alpha/H\beta$ flux ratio (i.e., Balmer decrement) can trace the dust extinction. When there is no dust in galaxies, the $H\alpha/H\beta$ ratios are expected to be 2.86 for star-forming galaxies (in the nominal case B recombination for $T = 10\,000\text{K}$ and $n_e \approx 10\text{ cm}^{-3}$, Osterbrock & Ferland 2006). Thus, flux ratios larger than these values indicate dust extinction.

Figure 12 shows that the color increases with the stellar mass. To reduce the influence of stellar mass when we compare color differences between high-metallicity and control samples, we select $9.5 < \log(M_*/M_\odot) < 10.0$ as comparison. From Figure 12, we can see that the high-metallicity sample tends to be redder than control sample in $g - r$ by ~ 0.13 dex, in NUV- r by ~ 0.2 dex and in $[3.4] - [12]$ by ~ 0.5 dex. The high metallicity sample has higher $H\alpha/H\beta$ ratio than control sample by ~ 0.3 dex. Using K-S test, we find that the high-metallicity and con-

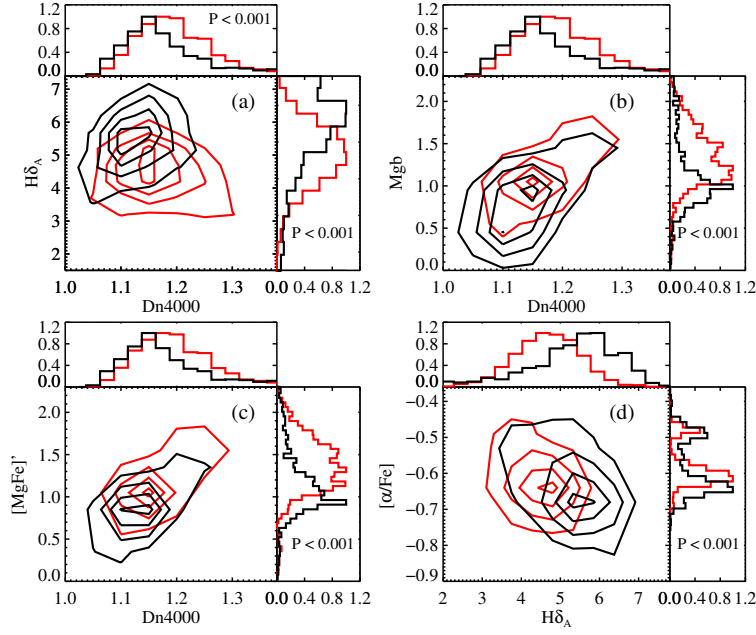


Fig. 8 The high-metallicity and control samples are shown in the plane of stellar absorption line index diagrams. (a) $H\delta_A$ as a function of D_n4000 ; (b) Mgb as a function of D_n4000 ; (c) $[MgFe]'$ as a function of D_n4000 ; (d) $[\alpha/Fe]$ as a function of $H\delta_A$. *Red contours* are the high-metallicity samples, and *black contours* are control samples.

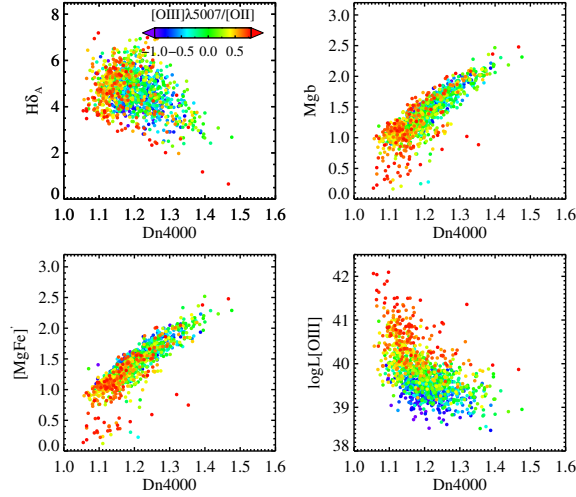


Fig. 9 $H\delta_A$ as a function of D_n4000 , Mgb as a function of D_n4000 , $[MgFe]'$ as a function of D_n4000 , and $\log [OIII]$ luminosity as a function of D_n4000 for the high-metallicity sample, the colorbar shows the $\log [OIII]/[OII]$ ratios.

trol samples have significant difference in distribution of colors. At the same time, there is a significant difference between the high-metallicity and control samples in $H\alpha/H\beta$ ratio. This difference in colors between the high-metallicity and control samples may be due to dust extinctions. Galaxies with high dust extinctions have moderately high metallicity (Heckman et al. 1998; Reddy et al. 2010).

Figure 13 shows that SFR, sSFR (SFR/M_*), $[\alpha/Fe]$ and D_n4000 as a function of stellar mass. From Figure 13, we can see that the high-metallicity sample has slightly lower SFR and sSFR on average than control sample by

~ 0.1 dex and ~ 0.1 dex, respectively. We also note that 0.1 dex is not large difference. However, we find that the high-metallicity and control samples have significant difference in the distribution of this two parameters by using K-S test. We can see that the high-metallicity sample has higher $[\alpha/Fe]$ than control sample by ~ 0.03 dex. Although 0.03 dex is not large difference, there is a significant difference between the high-metallicity and control samples in the distribution of α/Fe by using K-S test. Abundance of the α -elements can be used as indicator of timescales of star formation. The α -elements (such as mag-

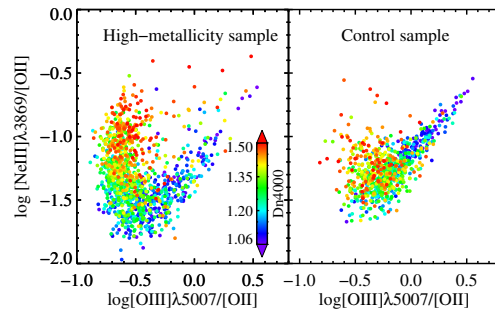


Fig. 10 The high-metallicity and control samples in the plane of $\log [\text{NeIII}]/[\text{OII}]$ as a function of $\log [\text{OIII}]/[\text{OII}]$ are colour-coded according to their $D_n,4000$ values, respectively.

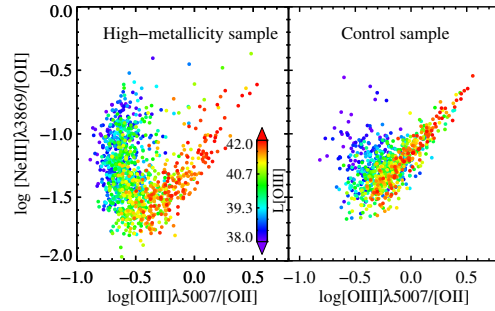


Fig. 11 The high-metallicity and control samples in the plane of $[\text{NeIII}]/[\text{OII}]$ versus $[\text{OIII}]/[\text{OII}]$ are colour-coded according to $\log [\text{OIII}]$ luminosity, respectively.

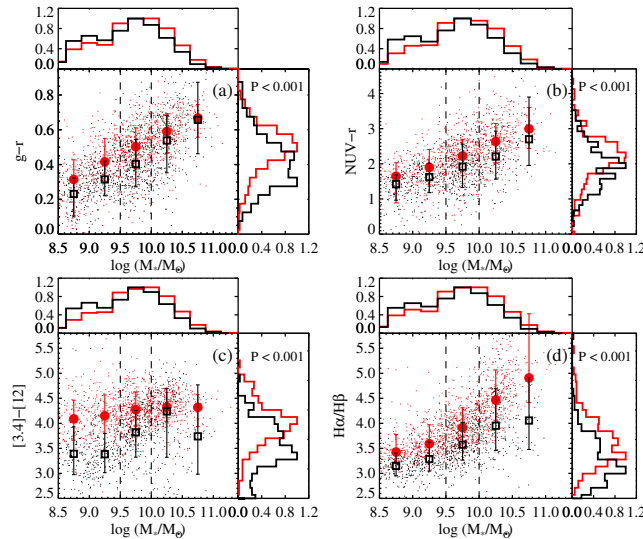


Fig. 12 The relation between color and stellar mass for the high-metallicity and control samples. (a) Optical colors versus stellar mass; (b) near-UV colors versus stellar mass; (c) mid-IR color versus stellar mass; (d) Balmer decrement ($H\alpha/H\beta$) versus stellar mass. *Red dots* are the high-metallicity samples, and *black dots* are control samples. *Large red circles* are medians of the high-metallicity samples. *Large black squares* are medians of control samples. The error bars are 16th and 84th percentiles in each bin. The histogram in each panel show the distribution of each parameter for the high-metallicity (*red line*) and control (*black line*) samples in a narrow mass range $9.5 < \log(M_*/M_\odot) < 10.0$.

nesium) are mainly from the Type II supernovae, which occur rapidly after a burst of star formation (timescales of $10^6 - 10^7$ yr) whereas the Fe-peak elements that are associated with the Type Ia supernovae, which lag behind by

at least 1 Gyr (Nomoto et al. 1984; Woosley & Weaver 1995). The high-metallicity sample has older stellar age and higher $[\text{Mgb}/\langle\text{Fe}\rangle]$ ratios than control sample. Our

results suggest that the high-metallicity samples may have shorter timescales of star formation.

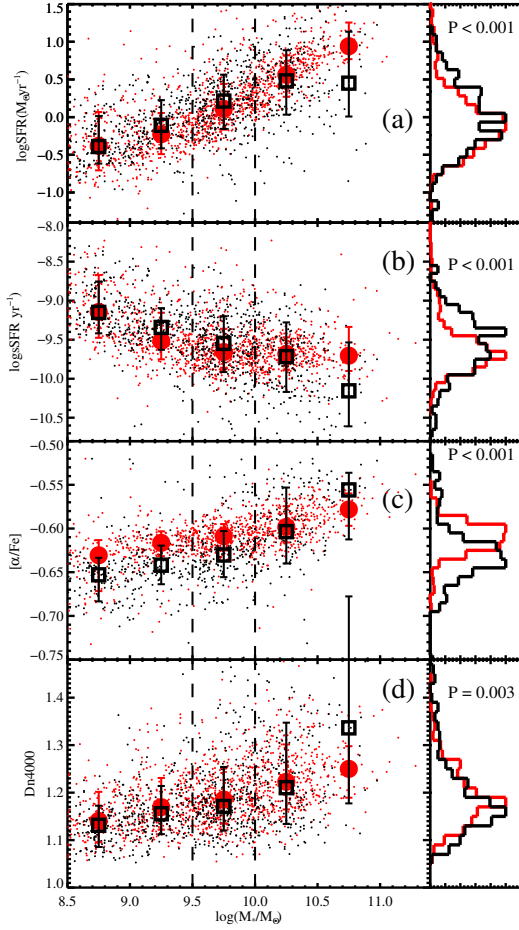


Fig. 13 SFR, sSFR, D_n4000 and $[\alpha/\text{Fe}]$ versus stellar mass for the high-metallicity and control samples. (a) SFR versus stellar mass; (b) sSFR versus stellar mass; (c) $[\alpha/\text{Fe}]$ versus stellar mass; (d) D_n4000 versus stellar mass. *Red dots* are the high-metallicity samples, and *black dots* are control samples. *Large red circle* is median of the high-metallicity sample. *Large black square* is median of control sample. The error bars are 16th and 84th percentiles in each bin. The histogram in each panel show the distribution of each parameter for the high-metallicity (*red line*) and control (*black line*) samples in a narrow mass range $9.5 < \log(M_*/M_\odot) < 10.0$.

3.7 Gas Properties

The atomic gas mass (M_{HI}) comes from the Arecibo Legacy Fast ALFA Survey (ALFALFA, Haynes et al. 2018), which provides data onto $\sim 31\,500$ galaxies at $z < 0.06$. Brown et al. (2015) studied the relationship between gas contents and star formation. They found that star formation activity is linked to the amounts of gas in galaxies. Therefore, we compare the amounts of atomic gas mass between the high-metallicity and control samples. Among the

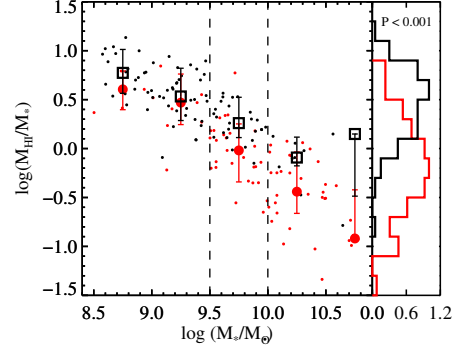


Fig. 14 Mass fraction of HI gas versus stellar mass. *Red dots* are the high-metallicity samples, and *black dots* are control samples. *Large red circles* are medians of the high-metallicity samples. *Large black squares* are medians of control samples. The error bars are 16th and 84th percentiles in each bin.

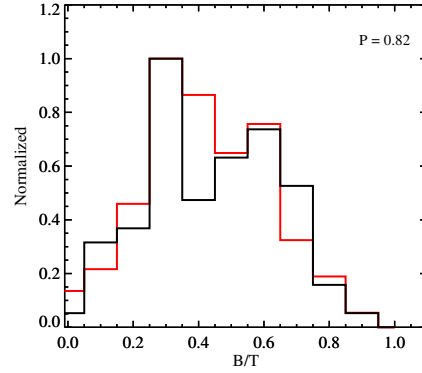


Fig. 15 The histogram of B/T for the high-metallicity and control samples. The *red histogram* is the high-metallicity sample, and *black histogram* is control sample.

1221 high-metallicity and 833 control samples, 78 high-metallicity samples and 89 control samples have HI detections. The relation between fraction of gas mass and stellar mass are shown in Figure 14. We find that the high-metallicity sample has lower fraction of gas than control sample by ~ 0.5 dex. Using K-S test, we find that the high-metallicity and control sample have significant difference in distribution of amounts of gas. The galaxies with high gas-phase metallicity may be due to their low HI gas fraction.

3.8 Structure Properties

The B/T is a tracer of structure of galaxies. Simard et al. (2011) provided a catalog of bulge and disk decomposition for 1.12 million galaxies in the SDSS. They used three different galaxies fitting models: a pure Sérsic model, an $n_b = 4$ bulge + disk model, and a Sérsic model (free n_b) bulge + disk model. In this paper, we only use a $n_b = 4$ bulge

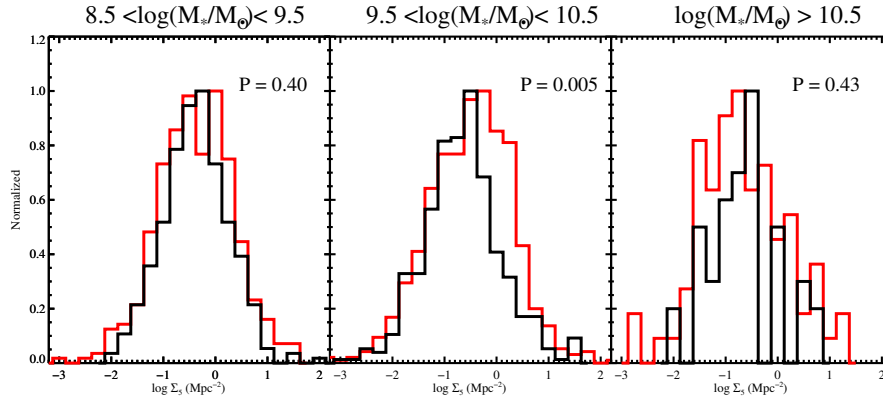


Fig. 16 The histogram of environment for the high-metallicity and control sample. The *red histogram* is high-metallicity sample, and *black histogram* is control sample.

+ disk model, and $PpS < 0.32$. We cross-match the high-metallicity sample with their catalog to get B/T. Figure 15 shows the distribution of B/T for the high-metallicity and control samples. Using K-S test, we find that the high-metallicity and control samples have no significant difference in distribution of B/T. At the same time, we find that most of the high-metallicity and control samples are disk-dominated galaxies (i.e., $B/T < 0.5$). Tremonti et al. (2004) used the concentration index ($C = R_{90}/R_{50}$), as a rough proxy for galaxy morphology. They found no correlation between the scatter in stellar mass–gas-phase metallicity relation and galaxy concentration. Thus, our results may suggest that there is no relation between gas-phase metallicity and galaxy morphology.

3.9 Environment

To study the relationship between galaxy activity and environment, there are a variety of methods to measure the environment of a galaxy. The most common way is to use Nth nearest neighbours technique. The projected density (Σ_5) is a sub-optimal environment metric (Mouhcine et al. 2007), especially when probing properties of gas content (e.g., Muldrew et al. 2012, Brown et al. 2018). Following Mouhcine et al. (2007), we use the following formula to estimate the environment density:

$$\log \Sigma_5 = \frac{1}{2} \log\left(\frac{4}{\pi d_4^2}\right) + \frac{1}{2} \log\left(\frac{5}{\pi d_5^2}\right), \quad (3)$$

where d_4 and d_5 are the projected distances to the fourth and fifth nearest neighbours within 1000 km s^{-1} (Baldry et al. 2006).

In order to avoid Malmquist bias and reach the minimum SDSS fiber separation when we estimate d_4 and d_5 , we only consider galaxies that are brighter than $M_r = -20$ mag, with separations of $50 h^{-1} \text{ kpc}$ (Li et al. 2009). The

sample is volume limited for galaxies brighter than $M_r = -20$, which is the density defining population (Baldry et al. 2006). The bright limit gives us a uniform density estimate that is applicable to our magnitude-limited sample over the full redshift range probed. The lower limit for projected distance is to avoid the galaxy itself was included when we estimate density. Furthermore, it is more important that the density estimate is not biased by SDSS fibre collisions. Moreover, it is also important to note that, for these density calculations, we have constructed a new reference sample using the SDSS Data Release 7 (DR7; Abazajian et al. 2009) which covers much larger area on the sky than do our samples of the high-metallicity/control sample. By these ways we have avoided for most of our sample the potential bias in the estimated densities. Thus, this ensures a high level of completeness, providing an adequate tracer sample to characterize the environment of our target sample.

Figure 16 shows the distribution of environment for the high-metallicity and control samples. The histogram of red color is the high-metallicity sample, and black color is control sample. Using K-S test, we find that the high-metallicity and control samples have no significant difference in distribution of environment. It is generally thought that the star formation may be related to the environment. Thus, one popular proposal is that environment affects metallicity. However, we find that there is not significant difference between the high-metallicity and control samples in the distribution of environment. Our results may suggest that there is no relation between environment and gas-phase metallicity.

4 SUMMARY

We use a sample of galaxies with unusually high gas-phase metallicity and compare their physical properties with control sample. Our main results are as follows.

1. The distributions of electron density and ionization parameter for the high-metallicity and control samples are significantly different. The high-metallicity sample tends to have higher electron density and lower ionization parameter than control sample.
2. The $g-r$, NUV- r , and mid-infrared [3.4]–[12] colors of the high-metallicity samples are statistically different from those of their control samples. These color differences may be due to the different dust extinctions, as evidenced by the Blamer decrement ($H\alpha/H\beta$).
3. The stellar population shows significant difference between the high-metallicity and control samples. The high-metallicity sample has old and metal-rich stellar population, as evidenced by D_n4000 , Mgb and MgFe. However, the control sample has young stellar population, namely low D_n4000 and high $H\delta_A$ value. From the D_n4000 vs. $H\delta_A$ panel, the control sample may experience recent star formation activity.
4. The high-metallicity and control samples have significant difference in the distribution of $[\alpha/Fe]$, namely $[Mgb/\langle Fe \rangle]$ ratio. The high-metallicity sample has higher $[Mgb/\langle Fe \rangle]$ ratio than control sample, which indicates that the high-metallicity sample has shorter timescales of star formation.
5. The HI gas fraction of the high-metallicity sample, on average, is lower than that of their control sample. The galaxies with high gas-phase metallicity may be due to their low HI gas fraction.
6. The distributions of environment have no significant difference between the high-metallicity and control sample, which may suggest that the environment has no effect on gas-phase metallicity.

Acknowledgements We are very grateful to the anonymous referee and editor for comments and suggestions that improved the manuscript. This work is supported by the National Key Research and Development Program of China (No. 2017YFA0402703) and the National Natural Science Foundation of China (Grant Nos. 11733002 and 11773013). The SDSS website is <http://www.sdss.org/>. The SDSS is managed by the Astrophysical Research Consortium for the Participating Institutions. The Participating Institutions are the American Museum of Natural History, Astrophysical Institute Potsdam, University of Basel, University of Cambridge, Case Western Reserve University, University of Chicago, Drexel University, Fermilab, the Institute for Advanced Study, the Japan Participation Group, Johns Hopkins University, the Joint Institute for Nuclear Astrophysics, the Kavli Institute for Particle Astrophysics and Cosmology, the Korean Scientist Group, the Chinese Academy of Sciences (LAMOST), Los Alamos National Laboratory, the Max-Planck-Institute for Astronomy (MPIA), the Max-Planck-

Institute for Astrophysics (MPA), New Mexico State University, Ohio State University, University of Pittsburgh, University of Portsmouth, Princeton University, the United States Naval Observatory, and the University of Washington.

References

- Abazajian, K. N., Adelman-McCarthy, J. K., Agüeros, M. A., et al. 2009, *ApJS*, 182, 543
- Andrews, B. H., & Martini, P. 2013, *ApJ*, 765, 140
- Baldry, I. K., Balogh, M. L., Bower, R. G., et al. 2006, *MNRAS*, 373, 469
- Baldwin, J. A., Phillips, M. M., & Terlevich, R. 1981, *PASP*, 93, 5
- Balogh, M. L., Morris, S. L., Yee, H. K. C., Carlberg, R. G., & Ellingson, E. 1999, *ApJ*, 527, 54
- Bian, F., Kewley, L. J., Dopita, M. A., & Blanc, G. A. 2017, *ApJ*, 834, 51
- Blanc, G. A., Kewley, L., Vogt, F. P. A., & Dopita, M. A. 2015, *ApJ*, 798, 99
- Blanton, M. R., Hogg, D. W., Bahcall, N. A., et al. 2003, *ApJ*, 594, 186
- Bothwell, M. S., Maiolino, R., Kennicutt, R., et al. 2013, *MNRAS*, 433, 1425
- Bothwell, M. S., Maiolino, R., Cicone, C., Peng, Y., & Wagg, J. 2016a, *A&A*, 595, A48
- Bothwell, M. S., Maiolino, R., Peng, Y., et al. 2016b, *MNRAS*, 455, 1156
- Brinchmann, J., Charlot, S., White, S. D. M., et al. 2004, *MNRAS*, 351, 1151
- Brooks, A. M., Governato, F., Booth, C. M., et al. 2007, *ApJ*, 655, L17
- Brown, T., Catinella, B., Cortese, L., et al. 2015, *MNRAS*, 452, 2479
- Brown, T., Cortese, L., Catinella, B., & Kilborn, V. 2018, *MNRAS*, 473, 1868
- Bruzual, A., G. 1983, *ApJ*, 273, 105
- Calura, F., Pipino, A., Chiappini, C., Matteucci, F., & Maiolino, R. 2009, *A&A*, 504, 373
- Chilingarian, I. V., Zolotukhin, I. Y., Katkov, I. Y., et al. 2017, *ApJS*, 228, 14
- Chisholm, J., Tremonti, C., & Leitherer, C. 2018, *MNRAS*, 481, 1690
- Cooper, M. C., Tremonti, C. A., Newman, J. A., & Zabludoff, A. I. 2008, *MNRAS*, 390, 245
- Dalcanton, J. J. 2007, *ApJ*, 658, 941
- Dalcanton, J. J., Yoachim, P., & Bernstein, R. A. 2004, *ApJ*, 608, 189
- Davé, R., Finlator, K., & Oppenheimer, B. D. 2012, *MNRAS*, 421, 98
- Dopita, M. A., Sutherland, R. S., Nicholls, D. C., Kewley, L. J., & Vogt, F. P. A. 2013, *ApJS*, 208, 10

- Edmunds, M. G. 1990, *MNRAS*, 246, 678
- Ellison, S. L., Patton, D. R., Simard, L., & McConnachie, A. W. 2008, *ApJ*, 672, L107
- Erb, D. K., Pettini, M., Shapley, A. E., et al. 2010, *ApJ*, 719, 1168
- Fosbury, R. A. E., Villar-Martín, M., Humphrey, A., et al. 2003, *ApJ*, 596, 797
- Gallazzi, A., Charlot, S., Brinchmann, J., White, S. D. M., & Tremonti, C. A. 2005, *MNRAS*, 362, 41
- Gao, Y., Wang, E., Kong, X., et al. 2018, *ApJ*, 868, 89
- Garnett, D. R. 2002, *ApJ*, 581, 1019
- Haynes, M. P., Giovanelli, R., Kent, B. R., et al. 2018, *ApJ*, 861, 49
- Heckman, T. M., Armus, L., & Miley, G. K. 1990, *ApJS*, 74, 833
- Heckman, T. M., Robert, C., Leitherer, C., Garnett, D. R., & van der Rydt, F. 1998, *ApJ*, 503, 646
- Hughes, T. M., Cortese, L., Boselli, A., Gavazzi, G., & Davies, J. I. 2013, *A&A*, 550, A115
- Hwang, H.-C., Barrera-Ballesteros, J. K., Heckman, T. M., et al. 2019, *ApJ*, 872, 144
- Kashino, D., & Inoue, A. K. 2019, *MNRAS*, 486, 1053
- Kauffmann, G., Heckman, T. M., Tremonti, C., et al. 2003a, *MNRAS*, 346, 1055 (Ka03)
- Kauffmann, G., Heckman, T. M., White, S. D. M., et al. 2003b, *MNRAS*, 341, 33
- Kehrig, C., Pérez-Montero, E., Vílchez, J. M., et al. 2013, *MNRAS*, 432, 2731
- Kewley, L. J., & Dopita, M. A. 2002, *ApJS*, 142, 35
- Kewley, L. J., Dopita, M. A., Sutherland, R. S., Heisler, C. A., & Trevena, J. 2001, *ApJ*, 556, 121 (Ke01)
- Kewley, L. J., Groves, B., Kauffmann, G., & Heckman, T. 2006, *MNRAS*, 372, 961
- Kewley, L. J., & Ellison, S. L. 2008, *ApJ*, 681, 1183
- Ko, J., Hwang, H. S., Lee, J. C., & Sohn, Y.-J. 2013, *ApJ*, 767, 90
- Kobulnicky, H. A., & Kewley, L. J. 2004, *ApJ*, 617, 240
- Komossa, S., & Schulz, H. 1997, *A&A*, 323, 31
- Lara-López, M. A., Hopkins, A. M., López-Sánchez, A. R., et al. 2013, *MNRAS*, 433, L35
- Larson, R. B. 1972, *Nature Physical Science*, 236, 7
- Larson, R. B. 1974, *MNRAS*, 169, 229
- Lee, G.-H., Hwang, H. S., Lee, M. G., et al. 2015, *ApJ*, 800, 80
- Levesque, E. M., & Richardson, M. L. A. 2014, *ApJ*, 780, 100
- Li, C., Gadotti, D. A., Mao, S., & Kauffmann, G. 2009, *MNRAS*, 397, 726
- Lian, J. H., Li, J. R., Yan, W., & Kong, X. 2015, *MNRAS*, 446, 1449
- Lian, J., Thomas, D., & Maraston, C. 2018, *MNRAS*, 481, 4000
- Lin, Z., Hu, N., Kong, X., et al. 2017, *ApJ*, 842, 97
- Mannucci, F., Cresci, G., Maiolino, R., Marconi, A., & Gnerucci, A. 2010, *MNRAS*, 408, 2115
- Martin, D. C., Fanson, J., Schiminovich, D., et al. 2005, *ApJ*, 619, L1
- Mouhcine, M., Baldry, I. K., & Bamford, S. P. 2007, *MNRAS*, 382, 801
- Muldrew, S. I., Croton, D. J., Skibba, R. A., et al. 2012, *MNRAS*, 419, 2670
- Nagao, T., Murayama, T., Shioya, Y., & Taniguchi, Y. 2002, *ApJ*, 567, 73
- Nagao, T., Maiolino, R., & Marconi, A. 2006, *A&A*, 459, 85
- Nomoto, K., Thielemann, F.-K., & Yokoi, K. 1984, *ApJ*, 286, 644
- Osterbrock, D. E. 1989, *Astrophysics of Gaseous Nebulae and Active Galactic Nuclei* (Mill Valley, CA: University Science Books)
- Osterbrock, D. E., & Ferland, G. J. 2006, *Astrophysics of Gaseous Nebulae and Active Galactic Nuclei* (2nd ed.; Sausalito, CA: University Science Books)
- Peeples, M. S., Pogge, R. W., & Stanek, K. Z. 2008, *ApJ*, 685, 904
- Peng, Y., Maiolino, R., & Cochrane, R. 2015, *Nature*, 521, 192
- Pettini, M., & Pagel, B. E. J. 2004, *MNRAS*, 348, L59
- Reddy, N. A., Erb, D. K., Pettini, M., Steidel, C. C., & Shapley, A. E. 2010, *ApJ*, 712, 1070
- Richard, J., Jones, T., Ellis, R., et al. 2011, *MNRAS*, 413, 643
- Richardson, C. T., Allen, J. T., Baldwin, J. A., et al. 2016, *MNRAS*, 458, 988
- Salim, S., Rich, R. M., Charlot, S., et al. 2007, *ApJS*, 173, 267
- Sánchez, S. F., Rosales-Ortega, F. F., Jungwiert, B., et al. 2013, *A&A*, 554, A58
- Sánchez, S. F., Barrera-Ballesteros, J. K., Sánchez-Menguiano, L., et al. 2017, *MNRAS*, 469, 2121
- Savaglio, S., Glazebrook, K., Le Borgne, D., et al. 2005, *ApJ*, 635, 260
- Scannapieco, C., Tissera, P. B., White, S. D. M., & Springel, V. 2008, *MNRAS*, 389, 1137
- Shimakawa, R., Kodama, T., Steidel, C. C., et al. 2015, *MNRAS*, 451, 1284
- Simard, L., Mendel, J. T., Patton, D. R., Ellison, S. L., & McConnachie, A. W. 2011, *ApJS*, 196, 11
- Thomas, D., Maraston, C., & Bender, R. 2003, *MNRAS*, 339, 897
- Thomas, D., Maraston, C., Schawinski, K., Sarzi, M., & Silk, J. 2010, *MNRAS*, 404, 1775
- Tinsley, B. M. 1980, *Fund. Cosmic Phys.*, 5, 287
- Tremonti, C. A., Heckman, T. M., Kauffmann, G., et al. 2004, *ApJ*, 613, 898
- Woolsey, S. E., & Weaver, T. A. 1995, *ApJS*, 101, 181
- Worthey, G., & Ottaviani, D. L. 1997, *ApJS*, 111, 377
- Wright, E. L., Eisenhardt, P. R. M., Mainzer, A. K., et al. 2010, *AJ*, 140, 1868
- Wu, P.-F., Zahid, H. J., Hwang, H. S., & Geller, M. J. 2017, *MNRAS*, 468, 1881
- Yates, R. M., Kauffmann, G., & Guo, Q. 2012, *MNRAS*, 422, 215
- Zhang, K., Yan, R., Bundy, K., et al. 2017, *MNRAS*, 466, 3217